Catalysis Science & Technology

Molecular Mechanisms of Methane Dry Reforming on Dual-Site Co3Mo3N Catalysts

Journal:	*Catalysis Science & Technology*
Manuscript ID	CY-ART-02-2021-000271.R1
Article Type:	Paper
Date Submitted by the Author:	29-Mar-2021
Complete List of Authors:	Manavi, Narges; Kansas State University College of Engineering, Tim Taylor Chemical Engineering Liu, Bin; Kansas State University, Chemical Engineering

Molecular Mechanisms of Methane Dry Reforming on Dual-Site Co_3Mo_3N Catalysts

Narges Manavi, and Bin Liu*

Tim Taylor Department of Chemical Engineering, Kansas State University, Manhattan, KS 66506

*Corresponding author:

Tel: (01)-785 532 4331

Email: binliu@ksu.edu

ABSTRACT

The catalytic performance of Co_3Mo_3N for dry reforming of methane (DRM) was investigated using periodic Density Functional Theory (DFT). The full mechanism revealed that $Co_3Mo_3N(111)$ activates both CH_4 and CO_2 at different catalytic regimes, which also facilitate CO production proceeds via COH and CHO intermediates. Aided by linear scaling relationships, steady-state microkinetic modeling confirms promising DRM reactivity thanks to the unique dual-site configuration on monolithic $Co_3Mo_3N(111)$ when compared to monofunctional transition metals. Efficient for C–H bond activation, $Co_3Mo_3N(111)$ is also effective at carbon residual removal due to facile CO_2 dissociation, and thus, tolerate surface C species. In synergy, the presence of moderate C and CH coverages help control surface O species. This work provides the insights into catalyst systems that contain two beneficial bifunctionalities for effective and durable DRM operations.

1. Introduction

Dry reforming of methane (DRM), as described by Eqn. (1), converts methane (CH_4) and carbon dioxide (CO_2) into a range of value-added chemicals including syngas,[1-4] methanol,[2] and sulfur-free diesel fuels;[5, 6] and thus engenders environmental and economic benefits. For DRM, however, carbon formation results in rapid catalyst deactivation, and remains a technological obstacle that hinders large-scale processes to realize its beneficial potentials.[7-9]

$$CH_4 + CO_2 \rightarrow 2CO + 2H_2, \quad \Delta H^{\circ}_{298} = 247\ kJ/mol \qquad (1)$$

Scheme 1. Parallel CH_4 and CO_2 conversion pathways (indicated by respective green and blue arrows) in the DRM reaction network. Potentially relevant intermediate steps and species are also presented. The hydrogenation/dehydrogenation steps are not explicitly labeled. CO and H_2 productions are also indicated by purple arrows.

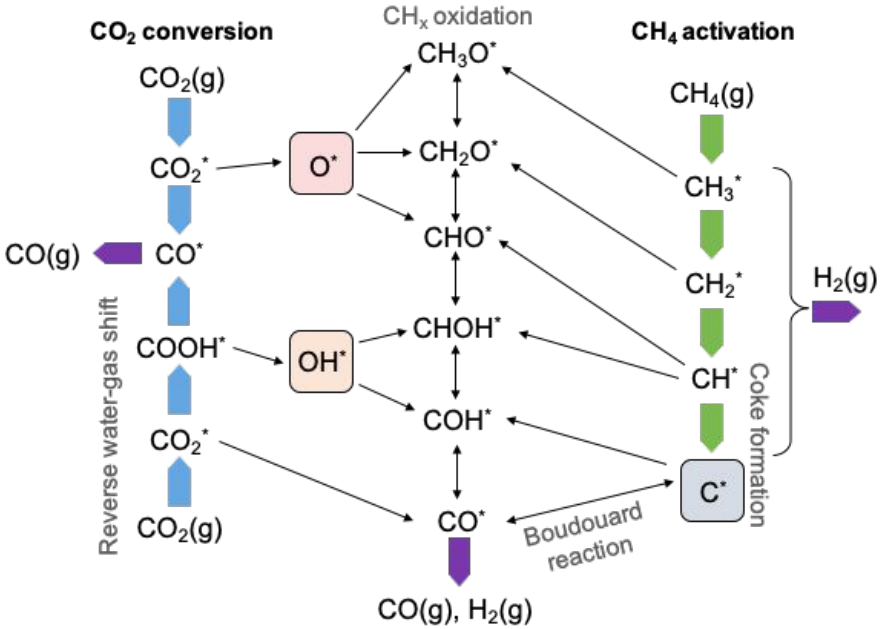

The reaction network derived from transition metal DRM catalysts based on various reviews on this topic is summarized in **Scheme 1**.[1, 10, 11] Akin to most C1 chemistries related to CH_4, the initial C–H bond activation is a rate-limiting step (RLS), where the CH_4 turnover frequency is often a reliable metric for the catalyst efficacy.[1] Specifically, Rostrup-Nielsen and Hansen [12] showed that the DRM rates on transition metals follow an order of: Ru > Rh > Ir >

Pt > Pd in a low-to-medium temperature range (773-923 K) and at the ambient pressure. For earth abundant metal catalysts such as nickel (Ni) and cobalt (Co), Ferreira-Aparicio and coworkers [13] demonstrated that supported Ni catalysts may outperform noble-metal Rh and Ru catalysts. However, Ni-based catalysts are notoriously susceptible to coke-related deactivation,[12] doping atoms like Sn may slow down carbon deposition at 1000 K.[14] Chen *et al*.[15] showed that coking on Co(111) at high temperatures.

Methane decomposition yielding H_2 at the metallic sites, according to Eqn. (2), can be presented in a stepwise sequence (green arrows in **Scheme 1**).[12, 16] In parallel, CO_2 activation (indicated by blue arrows in **Scheme 1**), supplies O or OH to manage surface carbonaceous (C, CH_x) intermediates.

Methane decomposition: $CH_4 \rightarrow C(s) + 2H_2, \Delta H^{\circ}_{298} = 75\ kJ/mol$ (2)

Reverse Boudouard: $C(s) + CO_2 \rightarrow 2CO\ , \Delta H^{\circ}_{298} = 171\ kJ/mol$ (3)

The reverse Boudouard reaction is able to convert solid-state carbon into CO via Eqn. (3). As such, higher temperatures (above 1000 K) generally favor carbon removal.[9] In addition, reverse water-gas shift (RWGS) reaction plays a role in DRM to produce H_2O as a side product. CO_2 chemisorption and dissociation are sensitive to surface structures, and can be enhanced by surface defects.[17, 18] To some extent, the C–O bond activation in CO_2 competes for the same active sites against CH_4 activation. Hence, there is a constraint on monofunctional transition metal catalysts to maintain a balance between C–H activation and C/CH conversion into CO.

There is plenty of evidence that DRM benefits from bifunctional catalysts. Commonly, CH_4 activation occurs at the metal sites, while CO_2 activation may take place on either acidic or basic oxide supports.[11] For instance, noble metal Pt catalysts supported on ZrO_2 promote CO_2 conversion during DRM while suppressing the carbon residue.[19, 20] The insights revealing what DRM mechanisms are enabled by specific metal-support functionalities can be leveraged to overcome the limiting DRM performance issues in future catalyst design endeavor.[10, 11]

Transition metal nitrides are metalloids with characteristic hybridization between the *d*- and 2*p*-orbitals of respective metal and N elements. These materials are less expensive and intrinsically coke resistant, and thus, have long been employed as alternatives to transition metal catalysts in many applications.[21] Many ternary metal nitrides exist as stable multi-

component monolithic materials, and add one more compositional parameter for fine-tuning of their catalytic properties. One notable example is Co_3Mo_3N, which has been long recognized as an outstanding material for ammonia synthesis.[22, 23] Recently, Fu *et al*. [24] demonstrated that Co_3Mo_3N exhibits promising reactivity toward DRM at temperatures below 873 K, and remains functional at up to 1073 K without significant catalyst deterioration. This appealing behavior has been attributed to the synergistic effects between Mo and Co components, high active site density, and the ability to balance CH_4 and CO_2 consumption rates.

Without a consensus on the DRM mechanism catalyzed by Co_3Mo_3N, in this work, periodic Density Functional Theory (DFT) was employed to reveal the origin of the DRM reactivity and coke resistance based on a close-packed Co_3Mo_3N facet that exposes coexisting Co and molybdenum nitride functional regimes, as geometric configurations among actives sites could play significant roles in directing the occurrence of RLS to mitigate site crowding and competition. With DFT calculations, we were also able to draw contrast between the Co_3Mo_3N ternary nitride and individual single crystalline Co(0001) and Mo_2N(110) surfaces to show that the superior performance indeed results from the synergistic effects stemming from the dual-site configuration. Moreover, the DRM kinetics on Co_3Mo_3N is quantified using a newly developed microkinetic model that accommodates the dual-site functionalities.

2. Methods

2.1 Catalyst models

The x-ray and neutron diffraction revealed that Co_3Mo_3N has a cubic $Fd3m$ lattice structure.[25] The bulk ternary Co_3Mo_3N nitride can be dissected into Co_8 octameric clusters and a Mo_3N framework with bridging nitrogen species (**Fig. 1a**).

The Co_3Mo_3N(111) surface exhibits patterned Co and molybdenum nitride (Mo_xN) domains (**Fig. 1d**). The neighboring Co domains are connected via a single corner Co_2 atom, while the Mo domains are isolated and bounded by three Co domains. Such alternating patterns help break up continuous active site domains that would be susceptible to the establishment of large-area carbon structures. Indeed, Rostrup-Nielsen *et al.*[26-28] suggested that interruptions of continuous domains help suppress coking because the size of active-site ensemble for coke formation is typically larger than what is needed for reforming. Cleavage along the (111) orientation may yield a number of possible close-packed configurations. Here,

the chosen facet represents the highest density of active sites; and was employed by Zeinalipour-Yazdi *et al*.[29] for the modeling of N_2 and H_2 adsorptions.

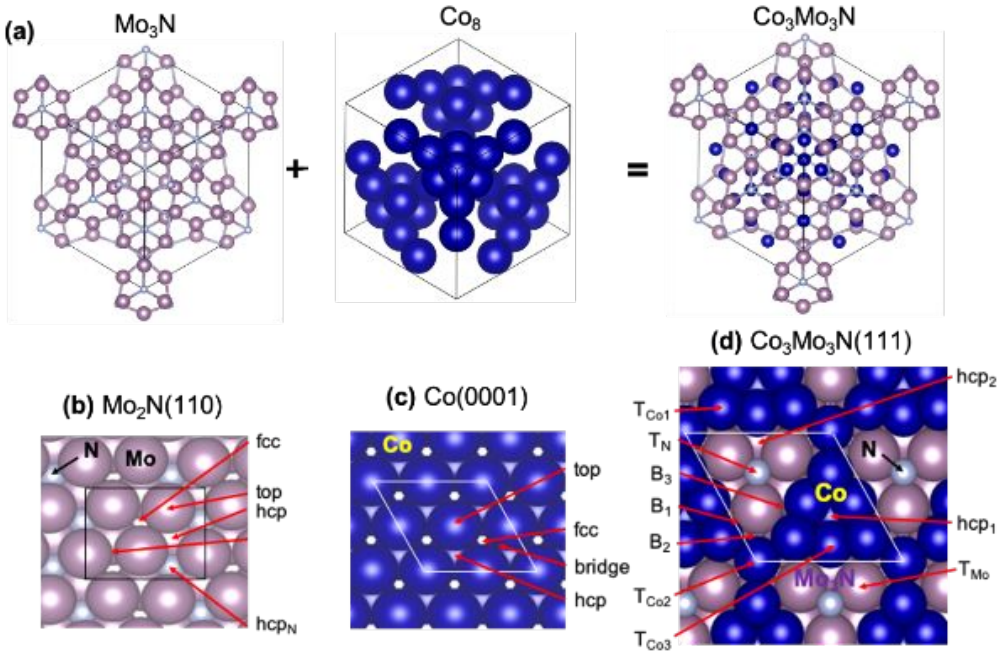

Fig. 1. (a) Dissection of the molybdenum nitride (Mo_3N) and cobalt in bulk ternary Co_3Mo_3N single crystal. (b-d) Top views the cleavage close-packed (111) orientation of Co_3Mo_3N, Co(0001), and (d) Mo_2N(110) surfaces, respectively. Accessible adsorption sites are also labelled. The Co, Mo, and N atoms are depicted in dark blue, pink, and light blue, respectively. The supercell boundaries are depicted with solid lines.

The Co domains in **Fig. 1d** exhibit a 3-fold symmetry. The center of the 3-fold site is denoted as hcp_1. Three distinct Co sites can be identified, denoted as $\mathbf{T_{Co_1}}$, $\mathbf{T_{Co_2}}$, and $\mathbf{T_{Co_3}}$. In the top layer, the Co_1 atom is bonded to one Co_2, two Co_3, and two Mo atoms. The Co_2 species is bonded with three Co_1 atoms and three Mo atoms. The Co_3 species is bonded to two Co_1, two Co_3, and two Mo atoms. All three Co sites are located at the boundary with the Mo domain, and the Co_1 species are undercoordinated relative to the other two Co sites in Co_3Mo_3N(111). Due to the varying numbers of coordination and ligand, each Co site is considered electronically distinct, corroborated by the *d*-band centers listed in **Table 1**. The *d*-band centers for all Co sites shift toward the Fermi level relative to Co atoms in Co(0001) (**Fig. 1c**) following an order of $Co_3 > Co_2 > Co_1$. Also, all Co sites are negatively charged (**Table 1**), indicating there is charge transfer from Mo to the nearest Co.

Table 1. The calculated *d*-band center (in eV) and Bader charge (in e) for Co(0001), Co_3Mo_3N(111), and Mo_2N(110). Surface site notations are consistent with Fig. 1d.

Surface	Atomic site	*d*-band center	Bader charge
Co(0001)	Co	-1.27	0
Co_3Mo_3N(111)	Co_1	-1.14	-0.10
	Co_2	-1.09	-0.37
	Co_3	-0.92	-0.26
	N	-	-1.17
	Mo	0.00	0.88
Mo_2N(110)	N	-	-1.44
	Mo	-0.04*	0.32*

* Such labeled values represent an average of the *d*-band center or Bader charge of different Mo atoms in the surface layer.

The Mo domains also exhibit 3-fold symmetry, consisting of three equivalent Mo atoms (labeled as T_{Mo}) and one bridging N in the top layer. The boundary sites are denoted as B_1 (Mo-Co_1), B_2 (Mo-Co_2), and B_3 (Mo-Co_3) for the Mo atoms bounded with different Co, respectively. The exposed bridging N, carrying a net charge of -1.17 e, is designated as T_N.

We also included the close-packed facets of respective Mo_2N (**Fig. 1b**) and Co (**Fig. 1c**) single crystals to represent the pure components of Co_3Mo_3N for later comparisons. The selection of Mo-terminated Mo_2N(110) facet is because this surface exhibits a similar atomic arrangement to the Mo domain of Co_3Mo_3N(111).

2.2 Density functional theory

All periodic DFT calculations were performed using the *Ab initio* Simulation Package (VASP).[30, 31] The generalized gradient approximation with the Perdew-Burke-Ernzerhof

functional (GGA-PBE) was used to account for the electron exchange and correlation.[32] The interactions between valence electrons and ion cores were described by the projector augmented wave (PAW) method,[33] with a cutoff for the expanded plane wave basis set up to 400 eV. The Brillouin-zone was sampled using the Monkhorst-Pack *k*-point mesh.[34] The convergence criterion for self-consistent iterations is 1.0×10^{-6} eV, with a residual force smaller than 0.02 eV/Å for ionic relaxations.

The binding energies (BE) reported in **Table 2** are defined according to Eqn. (4):

$$BE = E_{total} - E_{adsorbate\,(g)} - E_{surface}, \quad (4)$$

where E_{total} , $E_{adsorbate\,(g)}$, and $E_{surface}$ represent the total energies of the adsorbed surface species, adsorbate in gas phase, and clean surface, respectively. Furthermore, the energy barriers (E_a) and reaction energies (ΔE) for each elementary step reported in **Table 3** were obtained according to Eqns. (5-6):

$$E_a = E_{TS} - E_{IS}, \quad (5)$$

$$\Delta E = \sum_i E_{product,i} - \sum_j E_{reactant,j}, \quad (6)$$

where E_{TS}, E_{IS}, $\sum_i E_{product,i}$, and $\sum_j E_{reactant,j}$ are the total energies of the transition state (TS), the initial state (IS), and the summation of total energies for all product and reactant species, respectively. The total energies for the TS were obtained from the Climbing Image-Nudged Elastic Band (CI-NEB) and the dimer methods.[35, 36] All TS structures were confirmed with only one imaginary frequency.

All Gibbs free energies were estimated at 973.15 K and 1 bar by employing the standard statistical mechanical approach.[37] Under such conditions, the rate constants on Co_3Mo_3N(111), Co(0001), Mo_2N(110), and Ni(111) were evaluated based on the transition state theory (TST), see **Table S3** in ESI. Based on the order-of-magnitude analysis of the rate constants, a reduced DRM mechanism - consisting of 10 elementary steps, five gas phase species (CH_4, CO_2, CO, H_2, and H_2O), and eight surface intermediates (*, C, CH, CO_2, CO, O, H, and OH) - was proposed to obtain the turnover frequencies (see Appendix 1 of ESI). The rate

constants and equilibrium constants on $Co_3Mo_3N(111)$ and Ni(111) are summarized in **Table S4** in ESI.

The effective charges were obtained based on the Bader charge analyses [38]. The *d*-band centers (ε_d) were calculated as the first moment of the projected density of states (PDOS) relative to the Fermi level (ε_f) according to Eqn. (7):[39]

$$\varepsilon_d = \frac{\int_{-\infty}^{\varepsilon_f} \varepsilon \rho_d(\varepsilon)\, \mathrm{d}\varepsilon}{\int_{-\infty}^{\varepsilon_f} \rho_d(\varepsilon)\, \mathrm{d}\varepsilon}. \quad (7)$$

where ρ_d represents the PDOS.

3. Results and discussion

3.1 DRM intermediates on $Co_3Mo_3N(111)$ and site preference

The optimized surface bound intermediates CH_4, CO_2, H_2, CO, and H_2O at their preferred locations on $Co_3Mo_3N(111)$ are shown in **Fig. 2**. The binding energies (BE) and their preferred binding sites are listed in **Table 2**, along with the BE values on Co(0001) and $Mo_2N(110)$. The optimized structures on Co(0001) and $Mo_2N(110)$ are illustrated in **Fig. S1**-**S2** in ESI.

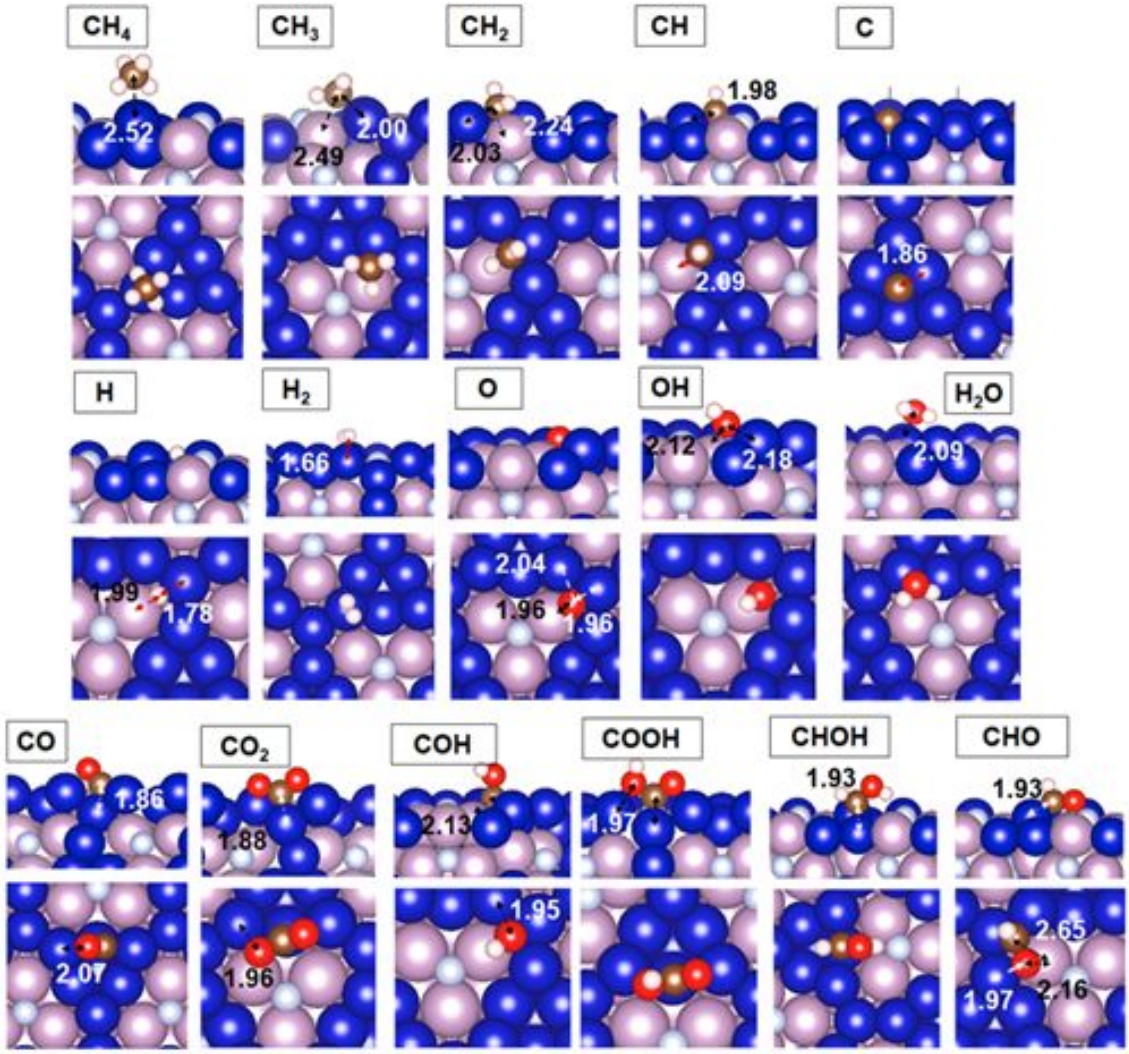

Figure 2. Optimized structures of the DRM intermediates on $Co_3Mo_3N(111)$. Atomic distances (in Å) are shown in dashed lines. The C, O, H, Co, Mo, and N atoms are depicted in brown, red, white, dark blue, pink, and light blue, respectively.

Table 2. Binding energies (BE in eV) and the preferred binding sites on $Co_3Mo_3N(111)$, Co(0001), and $Mo_2N(110)$.

Species	**$Co_3Mo_3N(111)$**		**Co(0001)**		**$Mo_2N(110)$**	
	Binding site	BE	Binding site	BE	Binding site	BE
CH_4	T_{Co_1}	-0.08	NP	-0.06	NP	-0.01
CH_3	T_{Co_1}	-1.93	fcc	-1.98	fcc	-3.01

CH_2	B_2	-4.49	hcp	-4.04	fcc	-5.22
CH	B_2	-7.07	hcp	-6.39	fcc	-7.41
C	hcp_1	-7.97	hcp	-7.04	hcp	-8.33
H_2	T_{Co_1}	-0.39	-	-	-	-
H	B_2	-2.87	fcc	-2.82	fcc	-3.31
O	B_2	-6.22	hcp	-5.77	fcc	-7.71
OH	B_1	-3.80	fcc	-3.48	fcc	-4.78
H_2O	T_{Co_1}	-0.67	top	-0.30	top	-0.77
CO	T_{Co_3}	-1.99	hcp	-1.69	hcp	-2.54
CO_2	T_{Co_3}	-1.50	hcp	-0.05	bridge	-0.82
COH	B_2	-4.70	hcp	-4.33	fcc	-5.13
CHO	B_2	-3.04	bridge	-2.21	hcp	-3.17
COOH	T_{Co_3}	-2.82	bridge	-2.29	hcp	-3.47
CHOH	T_{Co_3}	-4.27	fcc	-3.77	hcp	-4.52

Molecular CH_4 prefers the T_{Co_1} site, with a binding energy of -0.08 eV. This value is on a similar order of magnitude to the adsorption of closed-shell, nonpolar species on metal or metalloid surfaces. Still, as shown in **Table 2**, CH_4 binds slightly stronger than on Co(0001) and Mo_2N(110). At the T_{Co_1} site, the distance (2.52 Å) between CH_4 and the surface (a surface Co site) is the shortest. Electronically, the stronger CH_4 binding can be associated with the negatively charged, undercoordinated Co_1 site that facilitates electron back donation to the CH_4 anti-bonding orbitals.

CO_2 prefers the T_{Co_3} site and also binds stronger (-1.50 eV) than on both Co(0001) and Mo_2N(110). The chemisorbed CO_2 structure is bent; as illustrated in **Fig. 2**, its C atom is located at the T_{Co_3} site, and the two O atoms bind at the two neighboring T_{Co_1} sites.

Molecular H_2 prefers the T_{Co_1} site with a binding energy of -0.39 eV. The dissociation of H_2 is facile, then the dissociated H atom migrates to the B_2 site. Similar to CO_2, CO also prefers the T_{Co_3}site, with a binding energy of -1.99 eV. However, unlike CH_4 and CO_2, both H and CO bind stronger than on Co(0001) but weaker than on Mo_2N(110).

The carbonaceous CH_x intermediates (i.e., CH_3, CH_2, CH, and C) prefer the T_{Co_1}, B_2, B_2, and hcp_1 site, respectively. In fact for CH_x, a similar pattern has been observed elsewhere by Kua and Goddard on Pt(111).[40] The geometric interpretation of such site preferences is that CH_x (x = 0 – 3) favors the site that would satisfy the valence of the central C atom in CH_x. As to H and CO, CH_x (except for CH_3) species continue a trend where the binding energies are weaker on Co(0001), but stronger on Mo_2N(110).

The O, OH, and H_2O species prefer the respective B_2, B_1, and T_{Co_1} site. For the oxygenated carbon species, CHO prefers the B_2 site, whereas the primary binding sites for COH, COOH, and CHOH are B_2, T_{Co_3}, and T_{Co_3}, respectively. The binding energies of all above species also follow the order of Mo_2N(110) > Co_3Mo_3N(111) > Co(0001).

Based on their site preferences (**Table 2**), it is evident that DRM intermediates (except for C) predominantly occupy two types of active sites: (1) the negatively charged Co sites (T_{Co_1} or T_{Co_3}) for CH_4, CH_3, H_2, CO, CO_2, H_2O, CHOH, and COOH; and (2) the boundary sites (B_1 or B_2) for H, O, OH, CH, CH_2, COH, and CHO. Interestingly, we observed that all the reactants and products prefer one of the two Co sites: CH_4, H_2O, and H_2 on the T_{Co_1} site, while CO and CO_2 on the T_{Co_3} site. On the other hand, the reaction intermediates are more likely to occupy along the Co and Mo domain boundaries. Hence, the variety of Co_3Mo_3N(111) surface sites enables the fine differentiation of the site preference that potentially benefit DRM in terms of mitigating active site competition blockage.

The tuning of binding energies due to the electronic effects in alloys (including Co_3Mo_3N) is well-known and also crucial in catalytic applications such as NH_3 synthesis.[22] As reported in **Table 2**, we noted a familiar alloying effect for DRM catalysis as well, that is, a majority of DRM intermediates bind stronger on Mo_2N(110) but weaker on Co(0001) relative to Co_3Mo_3N(111), except for CH_4, CH_3, CO_2. In this case, stronger adsorptions of CO_2 (T_{Co_3}) and CH_4 (T_{Co_1}), particularly the latter, will favor the conversions of both chemically inert molecules thermodynamically.

Last, the binding energies of reaction intermediates on $Co_3Mo_3N(111)$ are also put to comparison with Ni(111), Ni(100), and Ni(211) as the benchmark systems.[41] Again, the stronger adsorptions of CH_4 and CO_2 on $Co_3Mo_3N(111)$ are considered as an enhancement favoring DRM. Among the reaction intermediates, only the atomic O binds notably stronger on $Co_3Mo_3N(111)$ than on all three Ni facets. The remaining CH_xO, CH_x, and OH bind similarly to the most active sites among all facets. Overall, we anticipate that the energetics the reaction routes will unlikely be very different from Ni. For the products, the bindings of H_2 and CO are also comparable to those on Ni;[41] thus, CO poisoning will not be a serious concern. However, H_2O, a side product of DRM, does bind stronger on $Co_3Mo_3N(111)$.

3.2 Elementary DRM steps on $Co_3Mo_3N(111)$

A total of 25 elementary steps can be adapted from **Scheme 1** to characterize DRM. The associated reaction energies (ΔE) and energy barriers (E_a) from DFT calculations are summarized in **Table 3**, with the TS structures depicted in **Fig. 3**. In addition, TS structures on Co(0001) and $Mo_2N(110)$ are shown in **Figures S3** and **S4** in the accompanying ESI.

Table 3. Reaction energies (ΔE in eV) and energy barriers (E_a in eV) on $Co_3Mo_3N(111)$, Co(0001), and $Mo_2N(110)$.

Elementary step		$Co_3Mo_3N(111)$		Co(0001)		$Mo_2N(110)$	
		ΔE	E_a	ΔE	E_a	ΔE	E_a
R1	CH_4 (g) + 2* ↔ CH_3* + H*	-0.08	0.65	0.01	1.02	-1.60	0.51
R2	CH_4 (g) + O* + * ↔ CH_3* + OH*	0.60	0.97	0.36	1.60	-0.08	1.89
R3	CH_3* + * ↔ CH_2* + H*	-0.46	0.51	0.13	0.72	-0.12	0.85
R4	CH_2* + * ↔ CH* + H*	-0.63	0.16	-0.33	0.22	-0.66	0.40
R5	CH* + * ↔ C* + H*	-0.02	0.96	0.40	1.13	-0.14	1.11
R6	CO_2 (g) + * ↔ CO_2*	-1.52	-	-0.05	-	-0.82	-
R7	CO_2* + * ↔ CO* + O*	-0.50	0.69	-1.03	0.46	-3.13	0.10

R8	C* + O* ↔ CO* + *	0.72	2.11	-0.57	1.84	1.14	2.76
R9	H* + O* ↔ OH* + *	0.67	1.38	0.35	1.27	1.51	1.99
R10	C* + OH* ↔ COH* + *	0.86	1.38	-0.14	1.75	0.99	2.26
R11	COH* + * ↔ CO* + H*	-0.81	0.71	-0.79	0.99	-1.36	1.27
R12	CH* +O* ↔ CHO* + *	1.34	1.65	0.90	1.59	1.95	2.13
R13	CHO* + * ↔ CO* + H*	-0.64	0.40	-1.08	0.14	-0.96	0.76
R14	CH* + OH* ↔ CHOH* + *	1.57	1.95	0.93	1.51	2.17	2.56
R15	CHOH* + * ↔ CHO*+ H*	-0.91	0.54	-	-	-1.73	0.41
R16	CHOH* + * ↔ COH*+ H*	-0.73	0.23	-	-	-1.32	-
R17	CO_2* + H* ↔ COOH* + *	1.28	1.43	0.23	1.38	0.37	0.93
R18	CO_2* + OH* ↔ COOH* + O*	0.61	0.98	-0.12	1.06	-	-
R19	COOH* + * ↔ CO* + OH*	-1.11	0.44	-0.98	0.24	-1.99	0.28
R20	CO_2* + C* ↔ 2CO*	0.21	1.80	-1.68	1.78	-1.99	1.42
R21	CO* ↔ CO (g) + *	1.99	-	1.69	-	2.54	-
R22	2H* ↔ 2* + H_2 (g)	1.26	-	1.09	-	2.13	-
R23	H* + OH* ↔ H_2O (g) + 2*	1.29	-	0.85	-	2.71	-

3.2.1 CH_4 activation

Both direct and O-assisted C–H bond activation of CH_4, as the RLS for DRM, were considered for DFT calculations. Xing *et al*. [42] reported that CH_4 dissociation can be promoted on O-covered IB group metals (e.g., Cu, Ag, Au). Most recently, the C–H bond activation were extended over transition metal-based facets, clusters, complexes, and oxides by Latimer and coworkers,[43] who revealed a linear correlation between the C–H bond activation energies and the cohesive energies of respective materials.

Direct CH_4 activation ($\boldsymbol{CH_4 + 2^* \rightarrow CH_3^* + H^*}$)**:** In R1, CH_4 was treated as a loosely bound molecule, due to its weak binding (-0.08 eV), prior to activation. The ΔE and E_a are -0.08 eV and 0.65 eV, respectively, producing CH_3 (T_{Co_1}) and H (B2). As illustrated in **Fig. 3** (TS1), the C–H bond activation occurs at the T_{Co_1}site, also preferred by the initial CH_4 adsorption. Also in **Fig. 3** (TS1), the C–H bond length in the TS is stretched to 1.66 Å. This barrier is significantly higher than on Mo_2N(110), but much lower than on Co(0001), as well as Pt (1.01 eV),[44] Ni(111) (0.91 eV),[41, 45] and Ni bimetallic alloys.[46]

O-Assisted CH_4 activation ($\boldsymbol{CH_4 + O^* \rightarrow CH_3^* + OH^*}$): The pre-adsorbed O species may participate in the abstraction of H from hydrocarbons to assist C–H bond activation (R2). As illustrated in **Fig. 3** (TS2), the participating O needs to move closer to the H by migrating from its preferred B_2 site to the B_1 site. The O–H distance decreases from 2.55 Å in the IS to 1.15 Å. DFT calculations showed that the O-assisted step is more endothermic (0.60 eV) than R1, with a barrier of 0.97 eV. A comparison between the direct and O-assisted C–H activation is also displayed in **Fig. 4a**. The higher C–H bond activation barrier can be attributed to the nonacidic nature of the C–H bond, and the energy compensation to displace O from its preferred site in the TS structure.

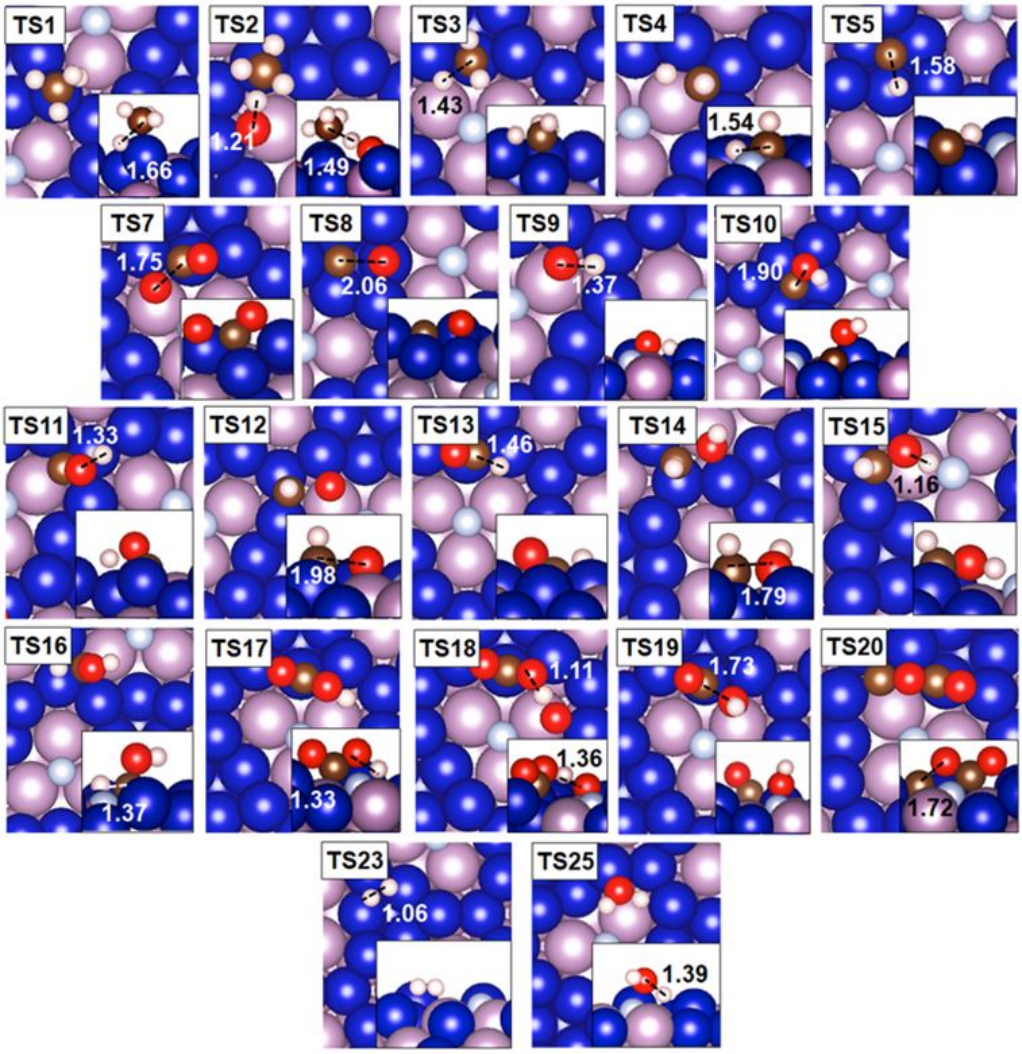

Fig. 3. Optimized transition state structures (corresponding to the notation in Table 4) on $Co_3Mo_3N(111)$. Side views are shown as the inset figure. The C, O, H, Co, Mo, and N atoms are depicted in brown, red, white, dark blue, dark pink, and light blue, respectively. Atomic distances (in Å) are shown in dashed lines.

CH_x decomposition ($\boldsymbol{CH_x \rightarrow CH_{x-1}^{*} + H^{*}}$): The decompositions of CH_3 and CH_2 (R3 and R4) occur with quite modest energy barriers at 0.51 and 0.16 eV, respectively. Facile CH_3 and CH_2 dissociation following the initial CH_4 activation is common, e.g., on Ni catalysts.[44-47] The energy barrier for CH decomposition (R5), however, increases substantially to 0.96 eV. Therefore, we anticipate that the CH could be a relevant species to CO formation. From the above analysis, a lumped CH_4 activation step was used in lieu of an explicit CH_4 decomposition sequence, with the overall kinetics determined by the energy barrier for the first C–H bond dissociation (see Appendix 1 in ESI).

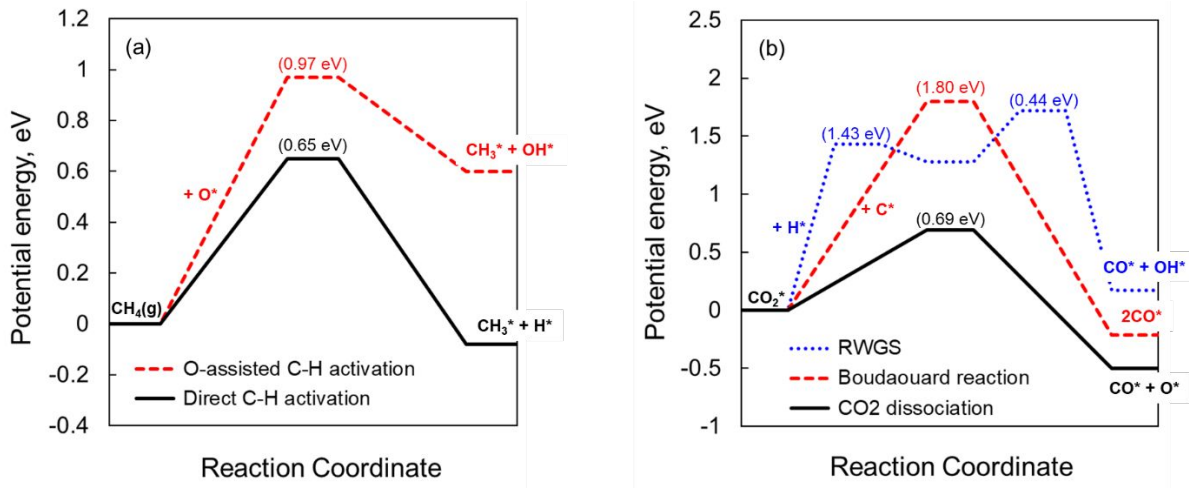

Fig. 4. Potential energy profiles for (a) direct (black) and O-assisted (red) C–H bond activation; (b) direct (black), H-assisted (blue), and C-assisted (red) CO_2 activation pathways on $Co_3Mo_3N(111)$. The energy barriers are labeled in parentheses.

3.2.2 CO_2 activation

Three CO_2 activation pathways, the direct, H-assisted, and C-assisted, were considered.

Direct CO_2 activation ($CO_2^* + * \rightarrow CO^* + O^*$): On $Co_3Mo_3N(111)$, R7 is moderately exothermic (-0.50 eV) with an energy barrier of 0.69 eV, with the C–O bond elongated to 1.75 Å (TS7). This barrier (0.69 eV) is similar to that (0.67 eV) on Ni(111),[41, 45] but lower than on Pt(111) (1.81 eV[44, 48]) and on NiSn [49].

H-Assisted CO_2 activation ($CO_2^* + H^* \rightarrow COOH^* \rightarrow CO^* + OH^*$): The H-assisted CO_2 activation (R17) is a critical step in RWGS,[50-52] in which H species (originating from CH_4 decomposition) is utilized to convert CO_2 into a carboxyl (COOH). However, on $Co_3Mo_3N(111)$, the R17 step is quite endothermic (1.28 eV in **Table 3**). In addition, an energy barrier of 1.43 eV is required to enable the O–H bond formation. This barrier is much higher than that on Ni(111) (1.13 eV[41, 45]) and on Pt(111) (0.75 eV [44]), respectively. Once COOH is formed, the C–O bond cleavage (R19) is rather exothermic (-1.11 eV) with a modest barrier of 0.44 eV.

Reverse Boudouard reaction ($CO_2^* + C^* \rightarrow 2CO^*$): The reverse Boudouard process (R20) converts solid carbon into CO using CO_2 as the co-reactant. On $Co_3Mo_3N(111)$, R20 is moderately endothermic (0.21 eV), versus Eqn. (3). Nevertheless, the energy barrier is prohibitively high at 1.80 eV when compared to Ni(111), i.e., 1.13 eV.[53]

The potential energy profiles depicting the three routes are summarized in **Fig. 4b**. The direct reaction pathway is clearly is the most competitive route for C–O bond cleavage and will be adopted to represent for CO_2 activation in the microkinetic model.

C and CH oxidation by O and OH. The oxidation pathways of C and CH species are less straightforward than CH_4 and CO_2 dissociations. Here, four pathways converting C and CH into CO were considered.

Direct C oxidation ($\boldsymbol{C^* + O^* \rightarrow CO^*}$): CO formation via the combination of atomic C and O (R8) takes place at the $\mathrm{T_{Co_3}}$ site and requires both atoms to migrate from their respective hcp_1 and B_2 sites to $\mathrm{T_{Co_3}}$ for C–O bond formation. This process is quite endothermic (0.72 eV) with a high energy barrier of 2.11 eV.

C oxidation via COH ($\boldsymbol{C^* + OH^* \rightarrow COH^* + * \rightarrow CO^* + H^*}$): An alternative path is to enable the C–O bond formation via the COH intermediate (R10), which then decomposes into CO and H (R11). The ΔE and E_a are 0.86 eV and 1.38 eV, respectively. The O–H bond cleavage is exothermic (-0.81 eV) with an energy barrier of 0.71 eV. The only limitation to this oxidation route is the surface concentration of OH species, which is produced from R9, with ΔE and E_a being 0.67 eV and 1.38 eV, respectively.

CH oxidation via CHO ($\boldsymbol{CH^* + O^* \rightarrow CHO^* + * \rightarrow CO^* + H^*}$): CH from incomplete CH_4 decomposition can be oxidized by O via the formyl (CHO) intermediate as in R12. This step is quite endothermic (1.34 eV) and will need to overcome an energy barrier of 1.65 eV for C–O bond formation. Still, the energy barrier related to CHO formation is lower than R8. The dissociation of CHO into CO and H is an exothermic step (-0.64 eV), with an energy barrier of 0.40 eV.

CH oxidation via CHOH ($\boldsymbol{CH^* + OH^* \rightarrow CH-OH^* + * \rightarrow CHO^*(COH^*) + H^* \rightarrow CO^* + 2H^*}$): Like C, CH can also be oxidized by OH via R14. However, the formation of CHOH is highly endothermic (1.57 eV), with a prohibitive energy barrier of 1.95 eV. The subsequent CHOH decomposition forming CHO is exothermic (-0.91 eV) with a moderate energy barrier of 0.54 eV. Alternatively, CHOH can form COH and H via C–H bond scission (R16), which is exothermic (-0.73 eV) with a low energy barrier (0.23 eV).

Based on DFT calculations, the RLS for all oxidation elementary steps involve the C–O bond formation.

3.2.3 Coke formation

The sources of coke formation are frequently attributed to CH_4 cracking and Boudouard reaction.[54] According to Nikoo and Amin,[55] CH_4 cracking is favored over the Boudouard reaction between 900 K and 1273 K. On $Co_3Mo_3N(111)$, the Boudouard reaction (reverse of R20 in **Table 3**) proceeds with a very high energy barrier 1.80 eV. Here, we focused on CH dissociation (R5) and CO decomposition (R8), both of which have lower energy barriers (0.96 eV and 1.39 eV) than that in the Boudouard pathway. With the CO desorption energy of 0.13 eV on $Co_3Mo_3N(111)$, the likelihood of CO decomposition (R8) is much diminished, as CO is more likely to desorb. Hence, CH_4 decomposition will be considered as the main mechanism for coke formation on $Co_3Mo_3N(111)$.

According to Bradford and Vannice,[1] carbon diffusion resulting in coke formation is sensitive to catalyst structures, especially the presence of large ensemble of metallic sites. Because the $Co_3Mo_3N(111)$ facet is dominated by interspersed Co and Mo_3N domains, large and continuous metallic domains for coke formation are absent. The electronic structures modulated by the interactions between the Co and Mo_3N domains also suppress coke formation. On $Co_3Mo_3N(111)$, the most preferred binding site for C is hcp1 with a binding energy of -7.97 eV. A stronger carbon binding on $Mo_2N(110)$ indicates that, on $Co_3Mo_3N(111)$, C atom likely prefers the Mo_3N over the Co domain. However, the top layer N species at the Mo hcp site blocks the access of carbon, hence, C binds at a secondary binding site (hcp_1). As a result, carbon binding is weakened on $Co_3Mo_3N(111)$. **Fig. 5** illustrates four possible carbon removal pathways on $Co_3Mo_3N(111)$ versus C–C bond formation producing the C_2 aggregates. We observed that the oxidation of C by OH should be the most competitive against C–C bond formation with the lowest energy barrier (1.38 eV versus 1.90 eV).

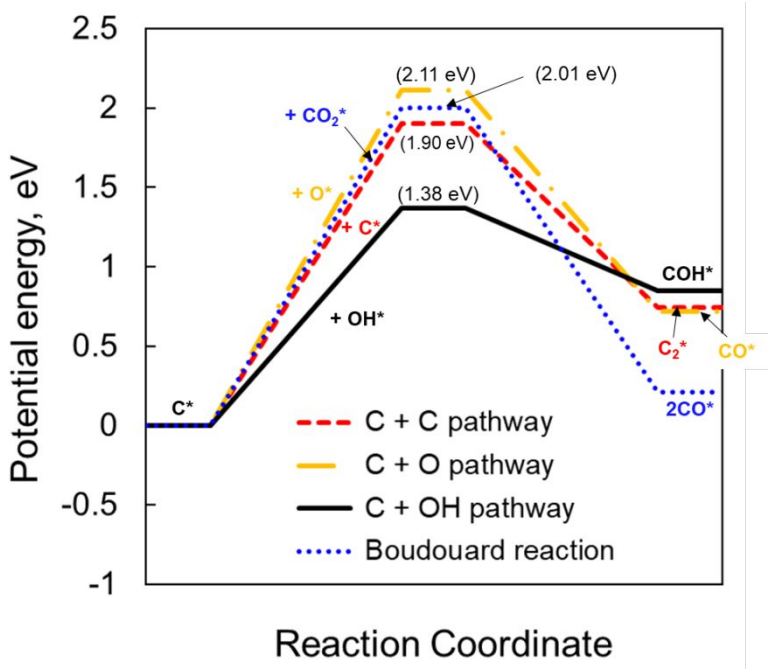

Figure 5. Coke formation pathway versus carbon removal pathways on $Co_3Mo_3N(111)$.

3.2.4 DRM pathways on $Co_3Mo_3N(111)$

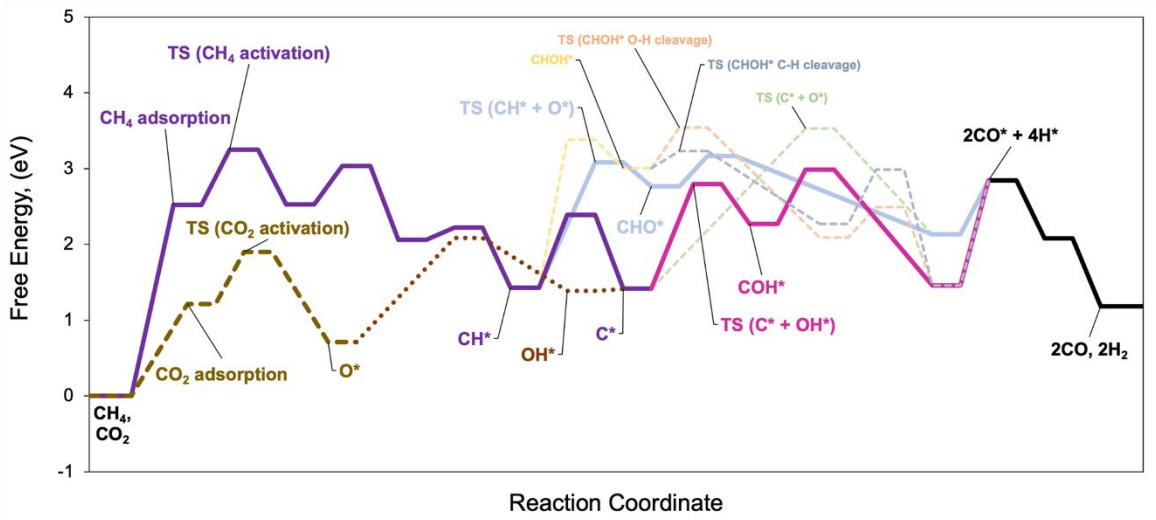

Fig. 6. The free energy profiles depicting DRM on $Co_3Mo_3N(111)$ - generated at 973.15 K and 1 bar. Gas phase CO_2 and CH_4 and clean surfaces are used as zero energy references. The main DRM routes are highlighted by thick lines including CO_2 (and subsequent OH formation) and CH_4 dissociation; C, CH oxidation via respective COH and CHO intermediates; and CO, H_2 formation that are illustrated in gold, purple, pink, blue, and

black, respectively. The less competitive pathways (e.g., CHOH formation and subsequent C–H and O–H bond dissociation) are represented in thin dashed or dotted lines.

Fig. 6 graphically depicts the free energy profile (at 973.15 K and 1 bar) of the DRM processes on $Co_3Mo_3N(111)$ based on the above analysis of DFT calculations. By adopting **Scheme 1**, we emphasize the parallel CH_4 and CO_2 conversion pathways (distinguished by respective solid purple and dashed gold lines) at the initial stage. It is evident that the initial CH_4 C–H bond activation is the RLS. In comparison, subsequent CH_x decompositions follow free energy downhill upon the initial activation, while the CO_2 dissociation free energy profile is much lower. The release of CO and H_2 as the gas phase products also follow steep free energy downhill due to significant entropy gains. The multiple CH or C oxidation pathways are also displayed. According to **Fig. 6**, indeed, the CH → CHO → CO (blue) and C → COH → CO (pink) routes are more competitive than the direct C oxidation and CHOH pathways. In fact, the conversions of C and CH, as the most abundant carbonaceous species, still resemble the oxidation pathways proposed on transition metal DRM catalysts.[1]

DFT calculations revealed that the sites in the Co_3Mo_3N Co domain can support parallel activations of CH_4 and CO_2 at two distinct sites; meanwhile, the bridge (Co-Mo) and hcp_1 sites permit C/CH oxidation to proceed without interference. Hence, the dual-site configuration in $Co_3Mo_3N(111)$ not only mitigates the site crowding and competition, but also allows both C–H activation and C–O bond formation to occur at their favoured sites.

The performance of DRM on Co(0001) and $Mo_2N(110)$ surfaces was also evaluated to better understand the synergy effect in $Co_3Mo_3N(111)$. In **Fig. S5**, the DRM consisting of only CH_4 activation and the most competitive CH oxidation pathways were shown, with the activation of CO_2 shown in a separate inset figure. On Co(0001) and $Mo_2N(110)$, the C–H bond activation occurs at the T_{Mo} and T_{Co} sites, respectively. The C–H bond activation on $Mo_2N(110)$ is more exothermic (-1.60 eV), with a lower energy barrier (0.51 eV) than on $Co_3Mo_3N(111)$. Still, the O-assisted C–H activations of CH_4 on Co(0001) and $Mo_2N(110)$ are not as competitive according to DFT calculations. This actually coincides with prior theoretical works, which already suggested that the C–H activation can sometimes be inhibited by the O and OH intermediates.[51, 56, 57]

The direct CO_2 dissociations on both Co(0001) and Mo_2N(110) proceed with lower energy barriers. This process is particularly facile on Mo_2N(110) with a barrier of only 0.10 eV. Morales-Salvador *et al*. [58] also suggested that Mo_2N is highly reactive toward CO_2 activation. In contrast, Co(0001) is more inert with an energy barrier of 0.46 eV. The binding energy of CO_2 on Co obtained by Wang and co-workers is -0.04 eV,[59] in good agreement with this work (-0.05 eV in **Table 3**). Wang *et al*. [60] stated that the CO_2 binding strength correlates with the corresponding *d*-band center of on transition metal surfaces. By extrapolating this behavior to the T_{Co_3} site in Co_3Mo_3N(111), the *d*-band of Co_3 atom on Co_3Mo_3N(111) is closer to the Fermi level. Also, Co_3 is more negatively charged than the Co atoms in Co(0001). Both factors result in more active Co sites in Co_3Mo_3N(111) than Co(0001) for CO_2 activation, and will ultimately favor DRM.

Facile CO_2 and CH_4 activations occur on Mo_2N(110) based on DFT calculations. In principle, this surface may be susceptible to either coking related to strong C and CH binding,[24] or the hindrance of O passivation. The most probable oxidation pathway on Co(0001) proceeds via the CH oxidation by OH, with a relatively low energy barrier of 1.51 eV, while all oxidation pathways are hindered on Mo_2N(110) due to the high reaction barriers (> 2 eV). Conclusively, as illustrated in **Fig. S5**, Mo_2N is predicted to lose its activity much more rapidly than Co and Co_3Mo_3N.

3.3 Microkinetic modeling of DRM on Co_3Mo_3N

The microkinetic model consists of 10 chemical species (i.e., CH_4, H_2, C, O, H, CH, OH, CO, H_2O, and CO_2) in 10 elementary steps (see Appendix 1 in ESI). CH_x (x = 2-3) dissociations following the initial CH_4 activation are quasi-equilibrated and were lumped into a single CH_4 decomposition step, producing CH, C, and H_2; while CO_2 activation produces CO and O directly. The carbonaceous species (CH and C) are converted into CO coupled with O and OH, respectively. A Mathematica script was developed according to Appendix 1 to obtain the TOF for CH_4 activation and surface coverage values at 1 bar and 973.15 K. The initial feed consists of equimolar CH_4 and CO_2 (i.e., $p_{CH_4} = p_{CO_2}$ = 0.5 bar) at a molar flow rate of 1 mol/s. The composition for the exiting gas stream consisting of CO, H_2, and H_2O, and the unreacted CH_4, CO_2, is determined by the equilibrium constant for Eqn. (1). The predicted TOFs were estimated based on a 55% CH_4 conversion as the function of BE_C and BE_O.

As shown in **Fig. S7(a-d)**, a series of linear scaling relationships were established to estimate BE_H, BE_{CH}, BE_{CO}, and BE_{OH} for H, CH, CO, and OH, as the key intermediates of the developed DRM microkinetic model. The qualities of linear scaling relationships and BEP are indicated by MAE, MAX values as discussed by Zaffran and coworkers.[61-63] The binding energies of H (BE_H) exhibit a high degree of correlation simultaneously with BE_C and BE_O (**Fig. S7a**), with a standard error of 0.11 eV. The corresponding parameters associated with BE_C and BE_O are 0.16±0.09 and 0.12±0.10 (both are unitless), respectively. Conventional linear scaling forms were adopted based on respective BE_C and BE_O for CH an OH according to Ref. [64].[64] Unlike other transition metal surfaces, the binding sites for C and O are uniquely distributed in different Co_3Mo_3N(111) regimes, i.e., the Co and the boundary sites. The acquired slopes of 0.76±0.07 (**Fig. S7b**) and 0.63±0.09 (**Fig. S7d**) for the 12 surfaces are in reasonable agreement to the values of 0.75 and 0.50,[64] and thus remain faithful to the empirical formulation $(n_{max} - n)/n$, where n_{max} and n represent the maximum H atoms bonded to C and O to fulfill their valency and the actual H atoms attached these central atoms. Because CO prefers to bind with its carbon end on transition metal and metalloid surfaces;[65] and thus, a correlation between BE_{CO} and BE_C was attempted. As shown in **Fig. S7c**, a linear scaling relationship does exist between BE_{CO} and BE_C, with a slope of 0.52±0.11 and a R^2 value of 0.92. Thus far, all key DRM intermediates appearing in the microkinetic model can be related to BE_C and BE_O.

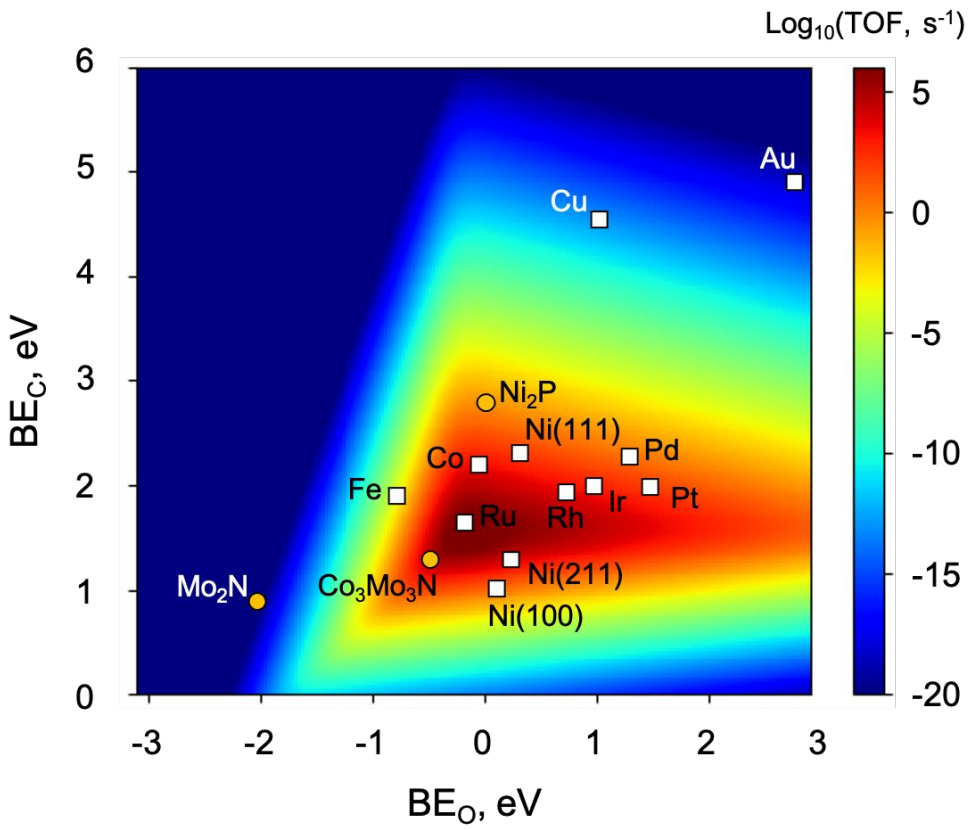

Fig. 7. Predicted $Log_{10}(TOF)$ (s^{-1}) for CH_4 activation according to Eqn. S34, as a function of BE_C and BE_O. The volcano heat map was generated using the linear correlations presented in Eqns. (S54-S58) as described in the Supporting Information. Reaction conditions used in the microkinetic model: T = 973.15 K, P = 1 bar, 55% CH_4 conversion, CH_4/CO_2 ratio = 1:1 at a molar flow rate of 1 mol/s. The transition metals are represented by white squares, while nitrides and phosphide are represented by yellow circles. The data point for Ni_2P was estimated based on Ref. [68].

A descriptor-based microkinetic model based on BE_C and BE_O adopts both the linear scaling and Bronsted-Evans-Polanyi (BEP) relationships derived for the initial C–H bond activation (see **Fig. S8** in ESI). As indicated in **Fig. 7**, a rather broad range of BE_O and BE_C values were covered with the chosen surfaces. Detailed reaction mechanism and the kinetic rate formulations are described in Appendix 1 in ESI.

The catalyst reactivities for both dual-site Co_3Mo_3N and single-site surfaces are characterized by the turnover frequencies (TOFs) of CH_4 C–H bond activation. The trend describing the DRM rates is illustrated by the heatmap in **Fig. 7**. The estimated $Log_{10}(TOF)$ values (in s^{-1}) on 15 close-packed surfaces (including those of Co_3Mo_3N, Mo_2N, and Ni_2P) are

explicitly identified on the heat map. The peak region encompasses Ru and Co_3Mo_3N. The majority of transition metals (e.g., Fe, Co, Ni, Rh, Ir, Pt, Pd) are dispersed in an area bounded by BE_C (1.0~2.8 eV) and BE_O (-0.9~1.5 eV). Au, Cu, and Mo_2N are located much further away corresponding to either much weaker or stronger BE_O and BE_C values. The microkinetic model predicts that Ru is among the most active single-site transition metals, followed by Co, Ni (both the 211 and 111 facets), and Rh; the next tier includes Ir, Pt, Pd, Ni(100), and Fe, with Cu and Au among the least active surfaces. This trend is reasonably consistent with the findings from Rostrup-Nielsen and Hansen, among other studies.[12, 66, 67]

The two metalloid catalysts, Mo_2N and Ni_2P, were also considered as single-site catalysts. Mo_2N, located in the lower left corner of **Fig. 7**, is also significantly less active than most monofunctional transition metals, as well as Co_3Mo_3N according to **Fig. S5**. Ni_2P, reportedly an effective DRM catalyst resistant to carbon coking,[68] displays a competitive Log_{10}(TOF), similar to that of Pd or Pt thanks to moderate BE_C and BE_O on Ni_2P(0001).

Co_3Mo_3N(111) is adjacent to Ru on the heatmap in a close proximity to the activity peak of the volcano. The high Log_{10}(TOF) exhibited on Co_3Mo_3N(111) can be attributed to the unique dual-site configuration. From literature, conventional DRM catalysts often rely on functional metal oxide supports (e.g., TiO_2,[19, 20] ZrO_2,[69] Ce/ZrO_2[70]) to acquire the key functionality for CO_2 activation for carbon residual removal.[10] Relative to Ru on the heat map, BE_C and BE_O are both stronger on Co_3Mo_3N(111). On Co_3Mo_3N(111), the C and CH intermediates preferentially occupy the Co site, while the O and OH occupy the Co-MoN boundary site. Hence, CH_4 activation and carbon oxidation kinetics proceed at the respective Co and Mo_3N domains simultaneously, which is an advantage for a catalyst consisting of a natural dual-site configuration.

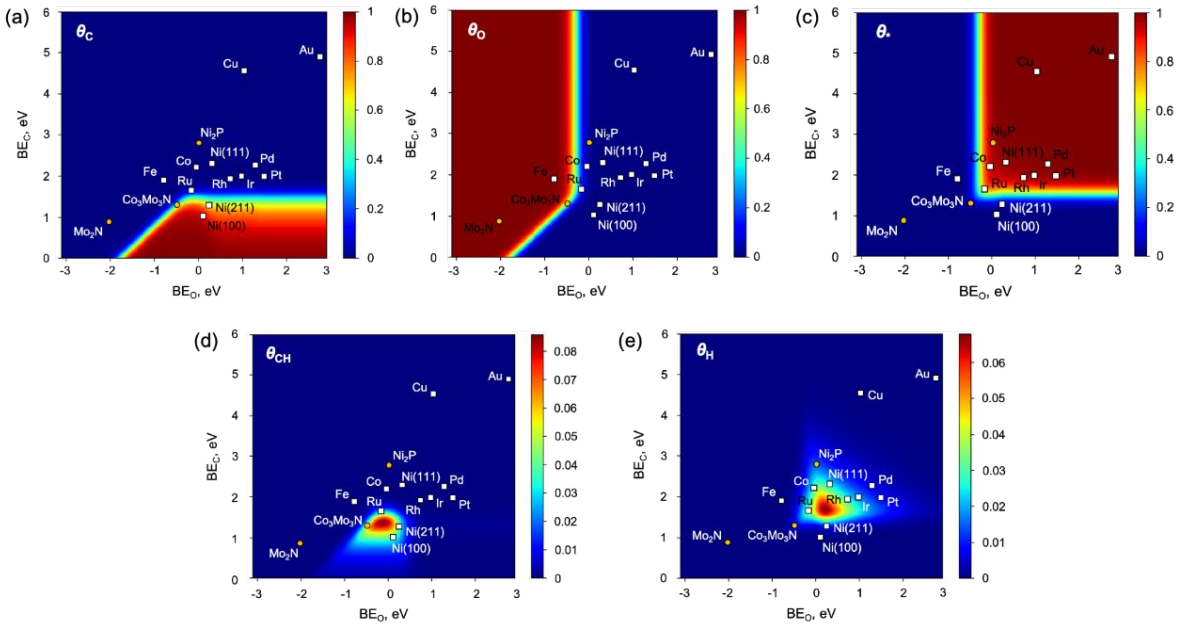

Fig. 8. Predicted surface coverage for (a) θ_C, (b) θ_O, (c) θ_*, (d) θ_{CH}, and (e) θ_H based on the same condition as in microkinetic modeling: T = 973.15 K, P = 1 bar, 55% CH_4 conversion, CH_4/CO_2 ratio = 1:1 at a molar flow rate of 1 mol/s. The transition metals are represented by white squares, while nitrides and phosphide are represented by yellow circles.

The predicted coverages of key DRM intermediates (i.e., C, O, CH, H, and *) from microkinetic modeling are summarized in **Fig. 8**. Atomic C and O are shown to be the most abundant surface intermediates (aka. MASIs). In **Fig. 8a**, θ_C is relevant mainly in the bottom-right corner, i.e., the strong C binding regime (BE_C < 1.5 eV). The absence of carbon coverage (in the lower left corner) suggests that strong O binding is able to counteract the dominance of C by occupying these active sites against C. This way, high θ_O values are located on the left-hand side of the heatmap (BE_O < 0.2 eV, see **Fig. 8b**), a strong O binding region. Similarly, deep in the strong C binding region, θ_O retreats and eventually yields to high θ_C (**Fig. 8a**) due to the competition from surface C species. The remaining area (**Fig. 8c**) bounded at BE_C > 1.5 eV and BE_O > 0.2 eV corresponds to surfaces that are mostly adsorbate-free.

Based on BE_C and BE_O, the Sabatier principle dictating DRM suggests that too strong C or O binding may hinder the C–H bond activation due to active site blockage by C or O; while weak C or O binding results in intrinsically high activation barriers. For instance, when coupled with the predictions shown in **Fig. 7**, the cause underlying low TOFs associated with Mo_2N and Fe - due to the excessively high θ_O (**Fig. 8a**) - becomes evident. On clean Au(111) and

Cu(111), the high C–H activation energy barriers reduce the TOF despite high open-site availability.

In fact, DRM rates on most close-packed surfaces shown in **Fig. 8a** are not severely interfered by C species. Then, we focused on three Ni single crystal facets - (111), (100), and (211) - to validate the performance of the established DRM mechanism, as coking is a well-known issue specially on the low-coordinated Ni sites.[53] Using **Fig. 8a**, θ_C indeed follows a decreasing order of Ni(100) > Ni(211) > Ni(111), suggesting that, under current modeling conditions, coking only becomes a serious issue in the presence of low-coordination sites. We also noted that, as BE_C increases in the order of Ni(111) < Ni(211) < Ni(100), the TOFs of all three Ni facets can be projected onto the opposite sides of the volcano plot along the vertical direction (**Fig. 7**). Hence, despite similar magnitudes of TOF, low coordination Ni sites benefits from higher C—H activation rates while Ni(111) benefit from less hindrance of coke formation.

Due to stronger C binding on Co_3Mo_3N(111) than on Ru, Co, Ni(111), as indicated in **Fig. 8a** and **8d**, there are small fractions of C and CH on Co_3Mo_3N(111) surface. Nevertheless, Co_3Mo_3N appears to tolerate such C presence. A plausible explanation is that: (i) C does not bind as strongly as on Ni(100); (ii) atomic O binds stronger than Ni, Ru, and Co. The left-shift of Co_3Mo_3N on the heatmap due to the latter is necessary to maintain sufficient active sites and sustain a high level of CH_4 conversion.

Lastly, this work also suggests that a moderate θ_C or θ_O will not necessarily be detrimental to catalyst performance; and may even be beneficial to sustain the progression of DRM on the surface. However, the optimal surface conditions and the potential of co-catalyst related to reaction intermediates on catalyst surface should be more thoroughly and systematically explored.

4. Conclusions

DFT calculations were performed to elucidate the molecular mechanisms of DRM on Co_3Mo_3N(111) so that the origins of its catalytic reactivity and coke resistance character can be understood. The proposed mechanism emphasizes initial parallel CH_4 and CO_2 activations, followed by oxidation and conversion of carbonaceous species into CO and H_2. The full mechanism revealed that Co_3Mo_3N(111) is capable of activating both inert molecules efficiently; and the dominant CO formation pathways proceed via the COH or CHO

intermediates. DFT calculations revealed the varying site preferences for reaction intermediates at different catalytic regimes of $Co_3Mo_3N(111)$. Generally, CH_4 and CO_2 activation favors the Co regime, while C oxidation and removal favor the boundary sites.

Trend analysis based on BE_C and BE_O (the catalytic descriptors) and linear scaling relationships confirmed that Co_3Mo_3N exhibits a superior DRM reactivity that is comparable to Ru. Also, Co_3Mo_3N performs significantly better than either of its single-site analogs (i.e., Mo_2N and Co). Steady-state microkinetic modeling revealed that the electronic properties and a unique dual-site configuration collectively enable a high turnover rate for C–H bond activation on $Co_3Mo_3N(111)$ and higher tolerance for surface C species due to facile CO_2 dissociation. It is also likely that the presence of moderate C and CH species help manage a moderate O coverage on the surface as well. The synergistic interactions between the Co- and Mo nitride regimes make Co_3Mo_3N a promising candidate for durable DRM.

Author contributions

Bin Liu conceptualized the project. Narges Manavi carried out the DFT calculations described in this paper and wrote the original draft. Bin Liu also participated in manuscript editing and revisions.

Conflicts of interest

There are no conflicts to declare.

Acknowledgements

Acknowledgment is made to the Donors of the American Chemical Society Petroleum Research Fund under the contract No. 61436-ND5 for the support of this research. N. M. is thankful for the Sustainable Energy Award provided by Center of Sustainability Energy at Kansas State University. The authors are grateful for the supercomputing service provided by K-State Beocat Research Cluster funded in part by NSF grants CHE-1726332, CNS-1006860, EPS-1006860, and EPS-0919443; and the National Energy Research Scientific Computing Center (NERSC) under the contract No. DE-AC02-05CH11231.

Notes and references

1. M. C. J. Bradford and M. A. Vannice, *Catalysis Reviews - Science and Engineering*, 1999, **41**, 1-42.
2. J. H. Lunsford, *Catalysis Today*, 2000, **63**, 165-174.
3. J. R. Rostrup-Nielsen, J. Sehested and J. K. Nørskov, *Advances in Catalysis* 2002, ***47***, 65-139.
4. M. V. Iyer, L. P. Norcio, A. Punnoose, E. L. Kugler, M. S. Seehra and D. B. Dadyburjor, *Topics in Catalysis*, 2004, **29**, 197-200.
5. H. Er-rbib, C. Bouallou and F. Werkoff, *Energy Procedia*, 2012, **29**, 156-165.
6. H. Er-rbib, C. Bouallou and F. Werkoff, *Chemical Engineering Transactions* 2012, **29**, 163-168
7. J. M. Ginsburg, J. Piña, T. El Solh and H. I. De Lasa, *Industrial and Engineering Chemistry Research*, 2005, **44**, 4846-4854.
8. O. Muraza and A. Galadima, *International Journal of Energy Research*, 2015, **39**, 1196-1216.
9. S. Arora and R. Prasad, *RSC Advances*, 2016 ***6***, 108668-108688
10. C. Papadopoulou, H. Matralis and X. Verykios, in *Catalysis for Alternative Energy Generation*, eds. L. Guczi and A. Erdôhelyi, Springer New York, New York, NY, 2012, pp. 57-127.
11. D. Pakhare and J. Spivey, *Chemical Society Reviews* 2014, ***43***, 7813-7837.
12. J. R. Rostrup-Nielsen and J. H. B. Hansen, *Journal of Catalysis*, 1993, **144**, 38-49.
13. P. Ferreira-Aparicio, A. Guerrero-Ruiz and I. Rodŕiguez-Ramos, *Applied Catalysis A: General*, 1998, **170**, 177-187.
14. S. Chen, J. Zaffran and B. Yang, *ACS Catalysis*, 2020, **10**, 3074-3083.
15. S. Chen, J. Zaffran and B. Yang, *Applied Catalysis B: Environmental*, 2020, **270**, 118859.
16. M. C. J. Bradford and M. A. Vannice, *Applied Catalysis A: General* 1996, ***142***, 97-122.
17. H. J. Freund and R. P. Messmer, *Surface Science*, 1986, **172**, 1-30.
18. F. Solymosi, *Journal of Molecular Catalysis*, 1991, **65**, 337-358.
19. A. N. J. Van Keulen, K. Seshan, J. H. B. J. Hoebink and J. R. H. Ross, *Journal of Catalysis*, 1997, **166**, 306-314.
20. M. M. V. M. Souza, D. A. G. Aranda and M. Schmal, *Journal of Catalysis*, 2001, **204**, 498-511.
21. S. T. Oyama, Springer Netherlands, Dordrecht, 1996, pp. 1-27.
22. C. J. H. Jacobsen, *Chemical Communications*, 2000, 1057-1058.
23. R. Kojima and K.-i. Aika, *Applied Catalysis A: General*, 2001, **215**, 149-160.
24. X. Fu, H. Su, W. Yin, Y. Huang and X. Gu, *Catalysis Science and Technology*, 2017, **7**, 1671-1678.
25. S. K. Jackson, R. C. Layland and H.-C. zur Loye, *Journal of Alloys and Compounds*, 1999, **291**, 94-101.
26. J. R. Rostrup-Nielsen, *Journal of Catalysis*, 1984, **85**, 31-43.
27. J. R. Rostrup-Nielsen and I. B. Alstrup, *Studies in Surface Science and Catalysis*, 1988, **38**, 725-732.
28. J. R. Rostrup-Nielsen, *Studies in Surface Science and Catalysis*, 1991, **68**, 85-101.

29. C. D. Zeinalipour-Yazdi, J. S. J. Hargreaves and C. R. A. Catlow, *Journal of Physical Chemistry C*, 2016, **120**, 21390-21398.
30. G. Kresse and J. Hafner, *Physical Review B*, 1994, **49**, 14251-14269.
31. G. Kresse and J. Furthmüller, *Computational Materials Science*, 1996, **6**, 15-50.
32. J. P. Perdew, K. Burke and M. Ernzerhof, *Physical Review Letters*, 1996, **77**, 3865-3868.
33. G. Kresse and D. Joubert, *Physical Review B*, 1999, **59**, 1758-1775.
34. H. J. Monkhorst and J. D. Pack, *Physical Review B*, 1976, ***13***, 5188-5192.
35. G. Henkelman and H. Jónsson, *The Journal of Chemical Physics*, 1999, **111**, 7010.
36. G. Henkelman, B. P. Uberuaga and H. Jónsson, *The Journal of Chemical Physics*, 2000, **113**, 9901-9904.
37. T. N. M. Le, B. Liu and L. K. Huynh, *Journal of Computational Chemistry*, 2014, **35**, 1890-1899.
38. G. Henkelman, A. Arnaldsson and H. Jónsson, *Computational Materials Science*, 2006, **36**, 354-360.
39. B. Hammer and J. K. Nørskov, *Advances in Catalysis*, 2000, **45**, 71-129.
40. J. Kua and W. A. Goddard, *Journal of Physical Chemistry B*, 1998, **102**, 9492-9500.
41. C. Fan, Y.-A. Zhu, M.-L. Yang, Z.-J. Sui, X.-G. Zhou and D. Chen, *Industrial & Engineering Chemistry Research*, 2015, **54**, 5901-5913.
42. B. Xing, X. Y. Pang and G. C. Wang, *Journal of Catalysis*, 2011, **282**, 74-82.
43. A. A. Latimer, A. R. Kulkarni, H. Aljama, J. H. Montoya, J. S. Yoo, C. Tsai, F. Abild-Pedersen, F. Studt and J. K. Nørskov, *Nature Materials*, 2017, **16**, 225-229.
44. J. Niu, X. Du, J. Ran and R. Wang, *Applied Surface Science*, 2016, **376**, 79-90.
45. Y.-A. Zhu, D. Chen, X.-G. Zhou and W.-K. Yuan, *Catalysis Today*, 2009, **148**, 260-267.
46. K. Li, M. Jiao, Y. Wang and Z. Wu, *Surface Science*, 2013, **617**, 149-155.
47. H. Liu, B. Wang, M. Fan, N. Henson, Y. Zhang, B. F. Towler and H. G. Harris, *Fuel*, 2013, **113**, 712-718.
48. J. M. Ricart, M. P. Habas, A. Clotet, D. Curulla and F. Illas, *Surface Science*, 2000, **460**, 170-181.
49. U. Guharoy, E. Le Saché, Q. Cai, T. R. Reina and S. Gu, *Journal of CO2 Utilization*, 2018, **27**, 1-10.
50. I. M. Bodrov, L. O. Apel'baum and M. I. Temkin, *Kinetika L Kataliz*, 1967, **8**, 821-828.
51. E. Shustorovich and A. T. Bell, *Surface Science*, 1992, **268**, 397-405.
52. J. Wei and E. Iglesia, *Journal of Catalysis*, 2004, **224**, 370-383.
53. R. C. Catapan, A. A. M. Oliveira, Y. Chen and D. G. Vlachos, *The Journal of Physical Chemistry C*, 2012, **116**, 20281-20291.
54. Z. Bian, S. Das, M. H. Wai, P. Hongmanorom and S. Kawi, *ChemPhysChem*, 2017, **18**, 3117-3134.
55. M. K. Nikoo and N. A. S. Amin, *Fuel Processing Technology*, 2011, **92**, 678-691.
56. B. Baek, A. Aboiralor, S. Wang, P. Kharidehal, L. C. Grabow and J. D. Massa, *AIChE Journal*, 2017, **63**, 66-77.
57. J. S. Yoo, T. S. Khan, F. Abild-Pedersen, J. K. Nørskov and F. Studt, *Chemical Communications*, 2015, **51**, 2621-2624.
58. R. Morales-Salvador, Á. Morales-García, F. Viñes and F. Illas, *Physical Chemistry Chemical Physics*, 2018, **20**, 17117-17124.
59. Y. Ma, L. Hernández, C. Guadarrama-Pérez and P. B. Balbuena, *The Journal of Physical Chemistry A*, 2012, **116**, 1409-1416.

60. S. G. Wang, X. Y. Liao, D. B. Cao, C. F. Huo, Y. W. Li, J. Wang and H. Jiao, *Journal of Physical Chemistry C*, 2007, **111**, 16934-16940.
61. J. Zaffran, C. Michel, F. Auneau, F. Delbecq and P. Sautet, *ACS Catalysis*, 2014, **4**, 464-468.
62. J. Zaffran, C. Michel, F. Delbecq and P. Sautet, *The Journal of Physical Chemistry C*, 2015, **119**, 12988-12998.
63. J. Zaffran, C. Michel, F. Delbecq and P. Sautet, *Catalysis Science & Technology*, 2016, **6**, 6615-6624.
64. F. Abild-Pedersen, J. Greeley, F. Studt, J. Rossmeisl, T. R. Munter, P. G. Moses, E. Skúlason, T. Bligaard and J. K. Nørskov, *Physical Review Letters*, 2007, **99**, 016105.
65. M. Mavrikakis, B. Hammer and J. K. Nørskov, *Physical Review Letters*, 1998, **81**, 2819-2822.
66. D. Qin and J. Lapszewicz, *Catalysis Today*, 1994, **21**, 551-560.
67. G. Jones, J. G. Jakobsen, S. S. Shim, J. Kleis, M. P. Andersson, J. Rossmeisl, F. Abild-Pedersen, T. Bligaard, S. Helveg, B. Hinnemann, J. R. Rostrup-Nielsen, I. Chorkendorff, J. Sehested and J. K. Nørskov, *Journal of Catalysis*, 2008, **259**, 147-160.
68. U. Guharoy, T. Ramirez Reina, E. Olsson, S. Gu and Q. Cai, 2019.
69. J. H. Bitter, K. Seshan and J. A. Lercher, *Journal of Catalysis* 1998, **1*76***, 93-101.
70. H.-S. Roh, K. Y. Koo, U. D. Joshi and W. L. Yoon, *Catalysis Letters*, 2008, **125**, 283-288.